JACS
JOURNAL OF THE AMERICAN CHEMICAL SOCIETY
pubs.acs.org/JACS
Article

Spatially Aware Diffraction Mapping Enables Fully Autonomous MicroED

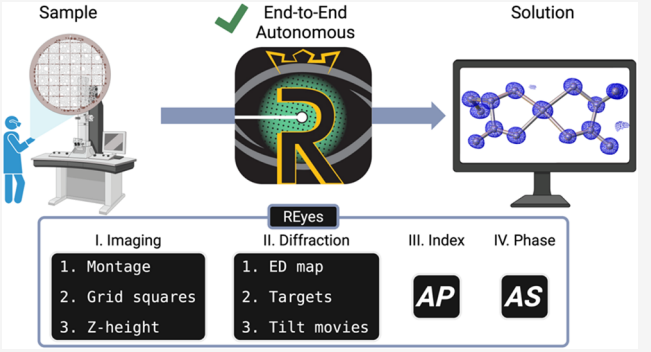
Dmitry B. Eremin, Kunal K. Jha, David A. Delgadillo, Hongyu Zhang, Samuel H. Foxman, Samuel N. Johnson, Niko W. Vlahakis, Duilio Cascio, Vincent Lavallo,* Jose A. Rodríguez,* and Hosea M. Nelson*

Cite This: J. Am. Chem. Soc. 2025, 147, 42299−42310

Read Online

ACCESS | Metrics & More | Article Recommendations | Supporting Information

ABSTRACT: In the hands of experts, microcrystal electron diffraction (microED, a 3D ED method) is a powerful tool for structural chemistry and chemical discovery. To expand the accessibility and utility of microED, we introduce Reciprocal Eyes (REyes), an autonomous and intelligent platform (available for academic use) that combines diffraction-based particle selection with real-time data processing to deliver crystal structures without human intervention. REyes spatially maps diffraction signal and autonomously selects crystallites of interest, relying on lattice-quality metrics to acquire and index high-resolution data sets from diverse compounds. Tested on four different transmission electron microscopes (TEMs), it consistently yields preliminary *ab initio* structural solutions from single crystallites of materials, peptides, metal complexes, natural products (NPs), and proteins.



INTRODUCTION

Despite being the subject of the 1937 Nobel Prize in Physics, electron diffraction (ED) has only recently emerged as a practical tool for the structural characterization of organic molecules. This contemporary renaissance, after nearly a century of dormancy, has been fueled by technological breakthroughs in continuous rotation data collection (microcrystal electron diffraction−microED, 3D ED), advanced transmission electron microscope (TEM) instrumentation,[1] and algorithmic innovations adapted from single-crystal X-ray diffraction (SCXRD).[2,3] These developments, originating largely from progress in CryoEM and SCXRD, have enabled ED to transition from a niche technique[4] to one with broad applications[5−10] across natural products (NPs) discovery,[11−13] polymer science,[14,15] metal−organic frameworks (MOFs),[16−20] and soft materials chemistry,[21−24] among others.

The growing use of ED has underscored the need for tools tailored specifically to microED, rather than retrofits of CryoEM or SCXRD workflows,[25,26] which are time-consuming and heavily reliant on human intervention.[27,28] Although semiautomated tools such as Instamatic,[29,30] RED,[31] SerialED,[32] and other "in-house" scripts and programs have emerged from academic laboratories, their adoption is limited by compatibility issues across diverse TEM platforms, or a requirement for highly specialized knowledge.[32−34] Meanwhile, commercial solutions from Thermo Fisher, Rigaku, JEOL, and ELDICO offer partially automated subroutines but are only available with proprietary hardware. None of the aforementioned solutions provides a truly autonomous end-to-end workflow from sample entry to a structure. Moreover, to the best of our knowledge, none of these platforms is designed to handle protein and small-molecule samples seamlessly.

We now describe a fully autonomous microED software suite: Reciprocal Eyes (REyes). It combines SerialEM-based ED acquisition with a Python package for intelligent real-time acquisition and analysis and is freely available for academic use. REyes replaces human-driven, time-consuming microED procedures, such as particle selection, with automated serial whole-grid diffraction mapping and particle selection based on diffraction quality, rather than real-space visualization (Figure 1A).[29,35]

A selection algorithm leveraging Patterson space criteria enables REyes to autonomously identify well-diffracting regions most likely to yield structural solutions from a single data set. When paired with automated data reduction (AutoProcess) and phasing (AutoSolve) modules, REyes

Received: June 25, 2025
Revised: October 20, 2025
Accepted: October 22, 2025
Published: November 10, 2025



Downloaded via UNIV OF CALIFORNIA SAN DIEGO on April 2, 2026 at 21:42:27 (UTC).
See https://pubs.acs.org/sharingguidelines for options on how to legitimately share published articles.

ACS Publications
© 2025 The Authors. Published by American Chemical Society

https://doi.org/10.1021/jacs.5c10751
J. Am. Chem. Soc. 2025, 147, 42299−42310

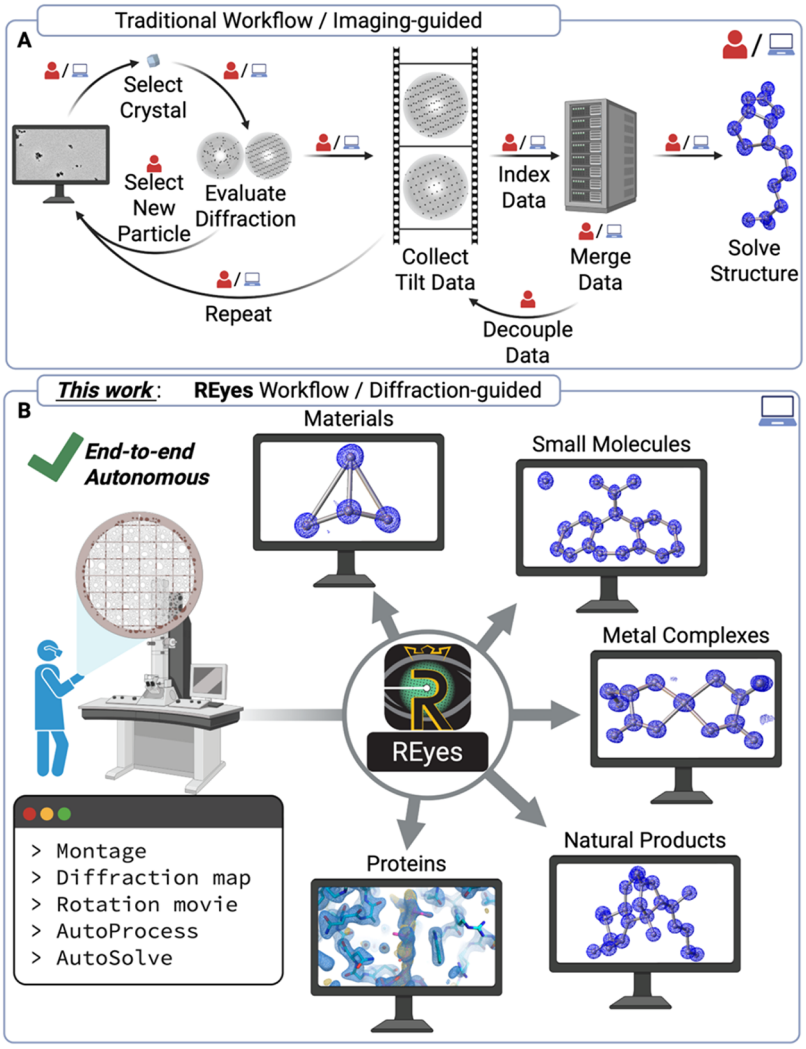


Figure 1. Traditional and fully autonomous microED workflows. (A) Traditional workflow using imaging mode and expert data curation. (B) Autonomous workflow using REyes, incorporating a diffraction atlas for spatially aware sample-independent data acquisition and automated indexing and phasing for preliminary structural solutions.

forms an end-to-end microED pipeline that matches or outperforms manual workflows completed in this study by experts (Figure 1B). We demonstrate its robustness across four uniquely configured TEMs at two universities and validate the platform by solving structures of (*S*,*S*)-salen ligand **1**, grossular **2**, biotin **3**, hexapeptide AVAAGA **4**, transition metal complex Cu(*D*-Ser)$_2$ **5**, citrinovirin **6**, mescaline **7**, carbamazepine **8**, and holo-lysozyme **9**.

RESULTS AND DISCUSSION

Automated Electron Diffraction. Recent automation regimes for microED have largely relied on an "imaging-first" strategy, where crystals are identified in real space prior to diffraction acquisition.[29−35] While these approaches increase throughput, computer vision methods require high-magnification imaging and systematically miss the thinnest crystals, which can be transparent in the imaging mode. Early embodiments of this strategy often yielded large fractions of low-quality data, partially mitigated by resolution-based quality metrics such as those introduced in Instamatic.[29] Moreover, existing automation packages still demand user intervention for target curation and parameter tuning, introducing bias, limiting scalability, and preventing fully autonomous workflows. To overcome these bottlenecks, we developed a "diffraction-first" automated serial diffraction paradigm, which comprises the foundation for REyes.

To facilitate autonomous data collection, we installed and calibrated the REyes pipeline on four TEMs equipped with field emission guns, two or more condenser lenses, and various scintillator-based or direct electron detectors. After installing REyes and calibrating the microscope for data acquisition, a single command triggers a fully automated sequence. It commences with the SerialEM-driven acquisition of an initial imaging atlas at low magnification (~150×), enabling subsequent processing stages. Grid squares are identified on this atlas using a segmentation algorithm,[36] locating grid squares with both low and high particle densities (Figure 2A). This information is communicated to the microscope, which adjusts the eucentric height for all grid squares by using an eucentric plane regression with only five selected points (Figure 2B).

Once all areas of interest have been identified, the microscope enters diffraction mode, and REyes spatially maps diffraction from designated areas of the grid. This step, akin to continuous, unbiased serial electron diffraction,

https://doi.org/10.1021/jacs.5c10751
J. Am. Chem. Soc. 2025, 147, 42299−42310

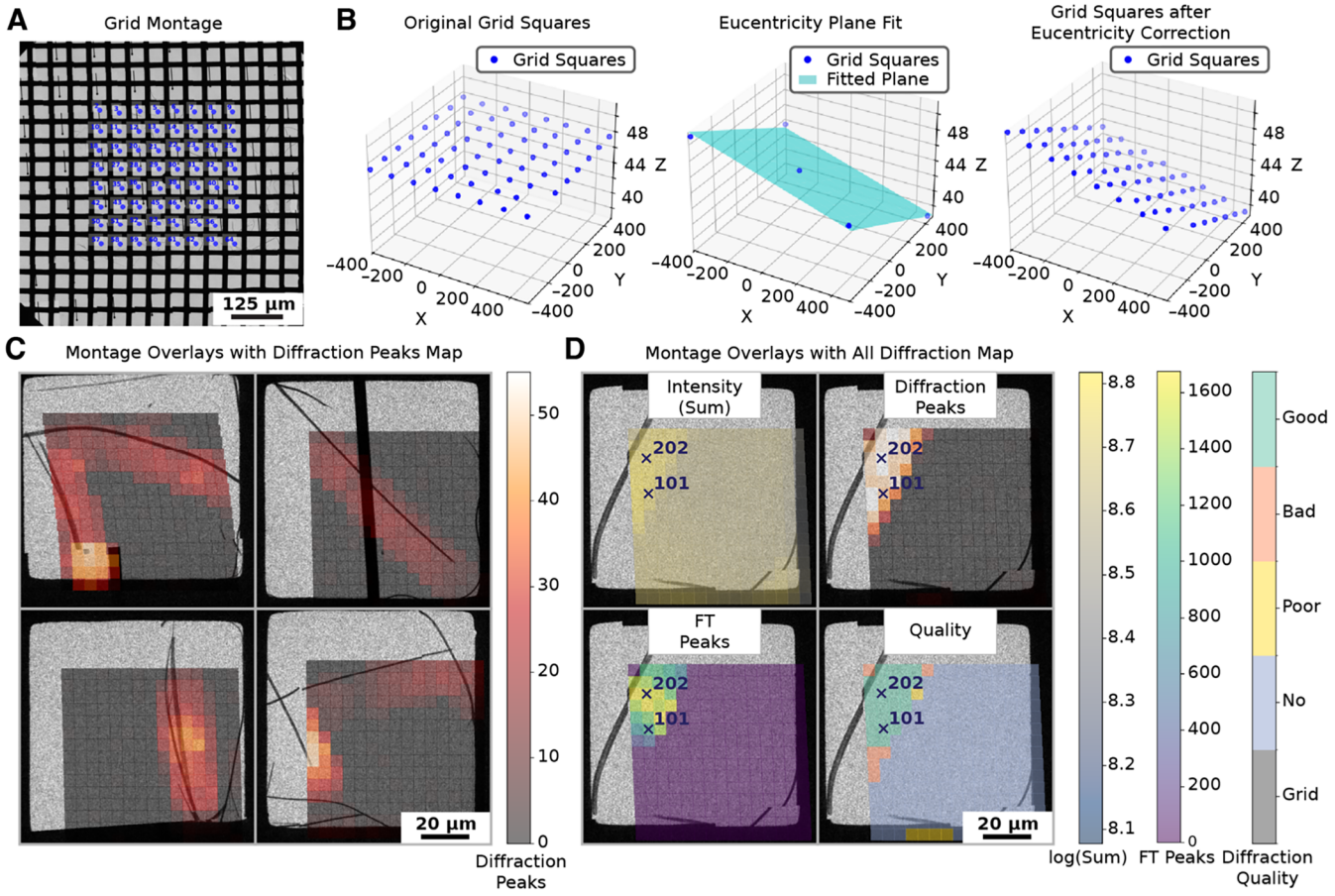


Figure 2. REyes workflow. (A) Grid montage (atlas) with identified grid squares. (B) Eucentric height adjustment step based on the eucentric plane regression. (C) Overlay of low-magnification images of selected grid squares with several detected diffraction peaks maps. (D) Example of selected grid square low-magnification image with intensity, number of diffraction peaks, LQP (lattice-quality peak) number, and diffraction quality maps obtained with on-the-fly data processing and possible acquisition locations. Note: All low-magnification images are offset compared with the diffraction space.

generates a map and conducts on-the-fly data analysis through the REyes monitoring system. Each pixel within this map corresponds to precise *x*-, *y*-, and *z*-coordinates, which link to sample diffraction data and metrics. Signal filtering applied to diffraction images enables real-time detection and counting of diffraction peaks in each pattern.

A map showing the number of detected diffraction peaks overlaid on the real-space image of the scanned grid area indicates a good correlation between the positions of the crystals and observed diffraction (Figure 2C). The total diffraction intensity of each pattern is also captured, which again correlates with the diffraction peak map (Figure 2D). However, lattice disorder and sample polycrystallinity could limit the utility of these maps for effective autonomous collection of high-quality data sets.

Robustness of high-quality target selection is achieved by analysis of diffraction patterns using peak-detection algorithms of fast Fourier transforms (FFTs) for individual diffraction snapshots. In the Patterson method, a Fourier transform (FT) calculated 3D map of interatomic vectors represents the autocorrelation of atomic positions.[37] Following this mathematical principle, we developed a 2D Patterson-like function of the reciprocal lattice itself, which computes the autocorrelation of detected diffraction spot positions.

We found that the number of peaks in the FFT of a diffraction pattern directly correlates with crystallite lattice quality, consistent with previous analyses of lattice defects and disorder.[38,39] REyes applies this 2D autocorrelation lattice-quality analysis to binarized diffraction images.[40] When a diffraction snapshot has a regular pattern, the FFT will have sharp, strong peaks, which we introduce as lattice-quality peaks or LQPs. For a random pattern or one representing the superposition of multiple lattices, the FFT will be smooth with few or no LQPs. The algorithm then computes the diffraction quality index (DQI), which is an LQP-to-diffraction-peak ratio. This autocorrelation-informed quality metric is used to classify each diffraction image and generate a comprehensive diffraction quality atlas. Regions exhibiting high DQI are then selected as targets for subsequent analysis, guiding both serial crystallography and single-crystal continuous rotation electron diffraction data collection (Figure 2D).

The core innovation of this approach is imaging directly in a diffraction space, which enhances throughput while prioritizing high-quality data collection. Because microscope time is often limited and diffraction is not an intrinsic property of all materials, such serial diffraction approaches are preferred over visual particle identification, which offers limited utility in microED workflows. REyes minimizes time spent on visual mapping, typically devoting less than 30 min per grid to real-space imaging. As the microscope continuously scans the grid in a continuous serial diffraction mode, a background algorithm classifies frames in real time according to diffraction

https://doi.org/10.1021/jacs.5c10751
J. Am. Chem. Soc. 2025, 147, 42299−42310

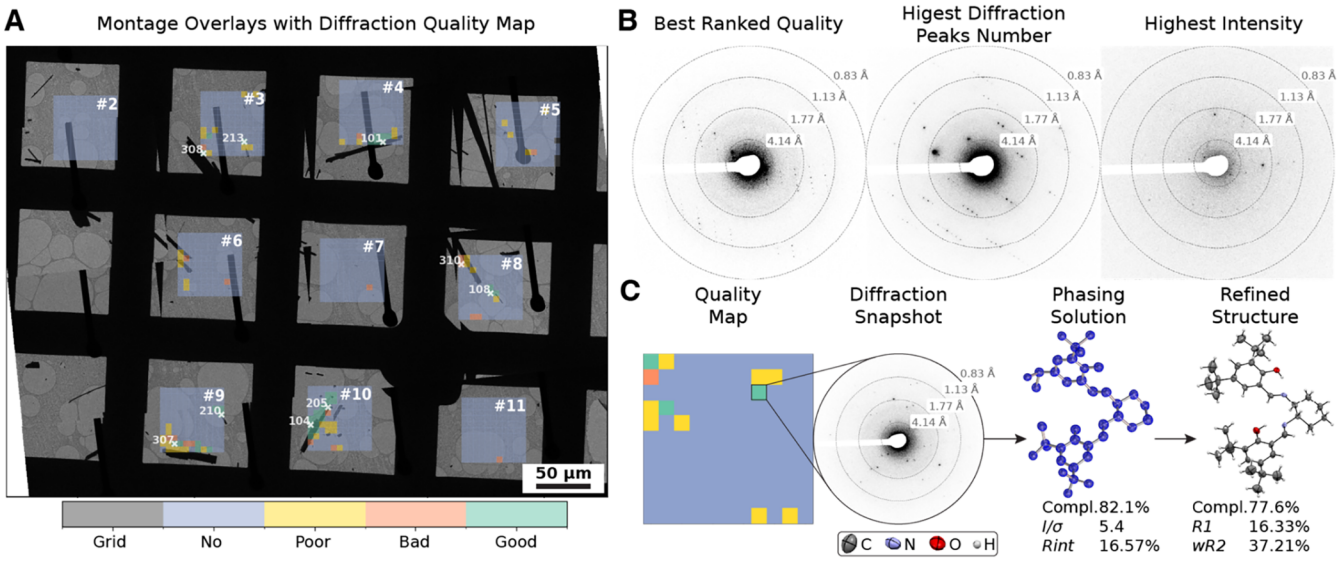


Figure 3. REyes, AutoProcess, and AutoSolve outcomes for a sample. (A) Diffraction quality map of the (*S*,*S*)-salen ligand **1** grid. (B) Diffraction snapshots of the highest-ranked targets by quality, peak number, and intensity. (C) Target 213: REyes 'Quality' diffraction map of a grid square led to a single-movie solution, diffraction snapshot at 0.8 Å max resolution of the target selected by REyes, *Fobs* map for *ab initio* preliminary solution at 0.8 Å, and refined structure of salen ligand **1**. Priority targets included items 101, 205, and 307 (Table 1).

quality metrics, including pixel intensity, diffraction peak count, and peak arrangement in FT, giving preference to frames with a high autocorrelation lattice-quality peak count (DQI). Upon completion of mapping, a ranked target list is autonomously compiled by REyes, highlighting regions with high DQI. This list can be customized based on quality thresholds to support targeted data acquisition. REyes directs the microscope to acquire tilt-series data over a specified angular range (Chart S1), typically ±50°, targeting ∼1° wedges per frame. With the latest hardware and counting detectors, a single tilt series could be collected under 60 s.

Spatially Aware MicroED Automation. Identifying crystals directly in diffraction space provides immediate feedback on diffraction quality but introduces a key challenge: redundancy. Because many crystals exceed the size of the electron beam, diffraction mapping without spatial context can lead to repeated acquisition from adjacent regions of the same large crystal, wasting microscope time and reducing data diversity. In contrast, computer vision helps to avoid redundancy but offers no information about diffraction quality across a crystal. To address these limitations, we implemented spatial awareness in REyes. By tracking the coordinates of all identified targets and enforcing a minimum spacing between acquisitions (typically ∼10 μm), REyes ensures that data are collected from distinct crystallites. This spatially informed diffraction mapping increases throughput, reduces redundancy, and improves sampling across the grid (Figure 3).

We initiated spatially aware REyes development using the (*S*,*S*)-salen ligand **1**.[41] We hypothesized that diffraction mapping within a narrow region (±200 μm from the stage origin) would typically be sufficient to determine its crystal structure. In this area, REyes identified 10 candidate locations (Figure 3A) and completed diffraction mapping within 2.3 h from initialization. The target list was curated to include the three best regions based on: (1) overall diffraction quality using DQI, (2) number of diffraction peaks, and (3) total frame-sum intensity. Each was selected with full spatial context to minimize overlap and ensure sampling of distinct crystals. This strategy, which incorporates three ranking criteria and spatial separation, effectively mitigates the target bias (Figure 3B).

As anticipated for (*S*,*S*)-salen ligand, (**1**), all prioritized targets exhibited distinct, high-quality diffraction patterns, surpassing 1.0 Å resolution. REyes autonomously acquired all 9 data sets using an Apollo direct electron camera in less than 30 min at 1°/s rotation rate. Because REyes is integrated with our AutoProcess package,[42] each acquired data set underwent on-the-fly autonomous processing using XDS. AutoProcess is initiated at the conclusion of each tilt-series. Of nine continuous rotation movies (±50° range) (Table 1), seven were successfully indexed to the anticipated unit cell and space group, one was indexed to the expected dimensions in a lower symmetry space group (Table 1, entry 8), and only one movie

Table 1. AutoProcess Indexing of Acquired MicroED Data for (*S*,*S*)-Salen Ligand (1)

entry	target	XDS space group	unit cell parameters (*a*, *b*, *c*, *α*, *β*, *γ*)	I/σ	$CC_{1/2}$	completeness at 0.8 Å
1	101	*P*222 (#16)	6.62, 17.92, 26.86, 90, 90, 90	7.75	98.5%	62.3%
2	104	*P*222 (#16)	6.60, 17.95, 27.12, 90, 90, 90	6.85	97.0%	69.5%
3	108	*P*1 (#1)	2.07, 5.17, 14.95, 85.56, 87.87, 83.55	1.73	82.1%	36.1%
4	205	*P*222 (#16)	6.59, 17.95, 27.15, 90, 90, 90	3.44	89.9%	67.8%
5	210	*P*222 (#16)	6.63, 17.85, 27.10, 90, 90, 90	5.50	97.7%	68.5%
6	213	*P*222 (#16)	6.62, 17.82, 27.28, 90, 90, 90	10.1	98.9%	82.1%
7	307	*P*222 (#16)	6.62, 17.80, 29.23, 90, 90, 90	1.47	17.4%	68.2%
8	308	*P*1 (#1)	6.62, 17.83, 31.00, 92.10, 93.15, 90.51	9.98	76.5%	27.8%
9	310	*P*222 (#16)	6.67, 17.88, 27.00, 90, 90, 90	1.82	68.9%	91.9%

https://doi.org/10.1021/jacs.5c10751
J. Am. Chem. Soc. 2025, 147, 42299−42310

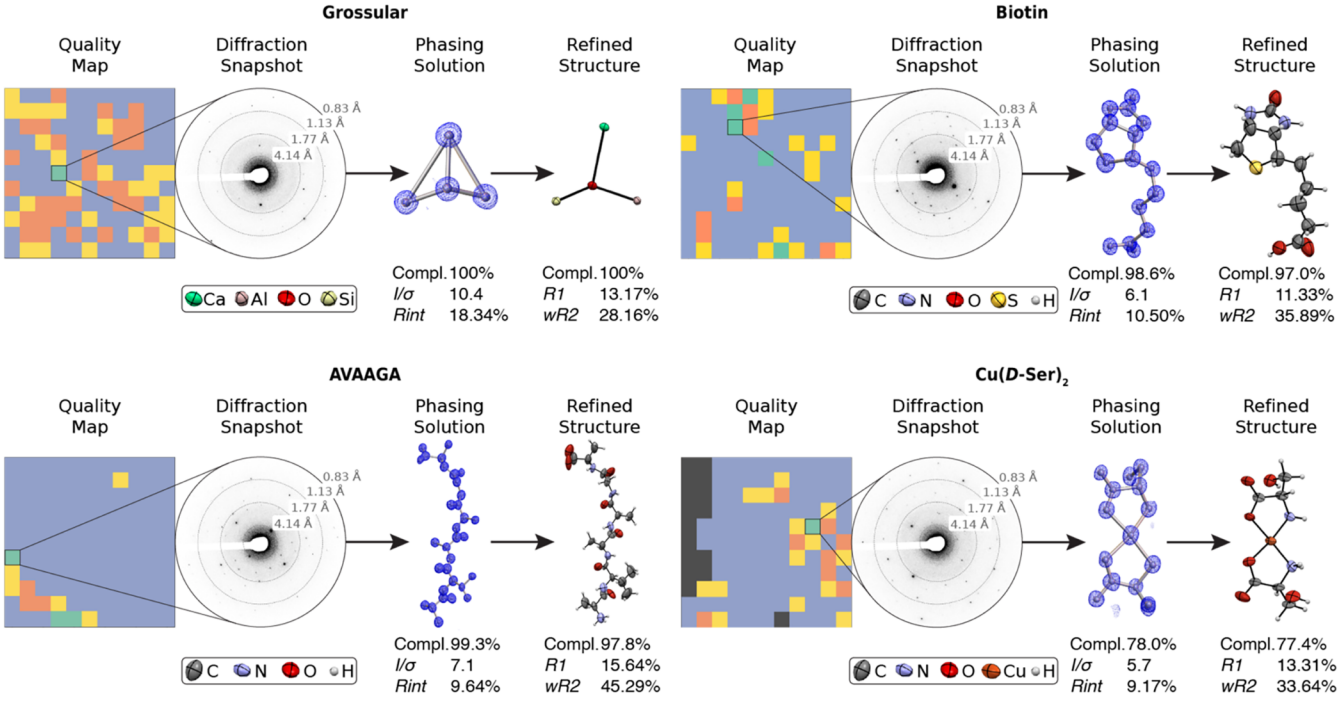


Figure 4. REyes, AutoProcess, AutoSolve, and refinement results of an autonomous microED acquisition. REyes "Quality" diffraction map of a grid square led to a single-movie solution, a diffraction snapshot at 0.8 Å max resolution of the target selected by REyes, a *Fobs* map for *ab initio* preliminary solution of 0.8 Å, and refined structure of grossular, **2**, biotin, **3**, AVAAGA peptide, **4**, and Cu(*D*-Ser)$_2$, **5** samples.

failed to yield the expected unit cell (Table 1, entry 3). On average, the indexing statistics reflected high-quality diffraction, with average I/σ = 5.3 and $CC_{1/2}$ = 81% including unsuccessful data sets; all selected targets were classified as "Good."

Following acquisition and indexing, all data sets were subjected to automatic phasing, using SHELXT and SHELXD,[34] referred to as AutoSolve. Target 213, identified in grid square #8 (Figure 3C), with the highest completeness at 82.1% (Table 1, entry 6), yielded an *ab initio* phasing solution at 0.8 Å from a single movie. A preliminary solution generated by SHELXD correctly elucidated the molecular structure and was manually kinematically refined (Figure 3C). The same grid was next analyzed using an Arctica/CETA-D microscope/camera configuration at cryogenic temperature and 0.12°/s rotation rate. The installation and adjustment of REyes-specific processing parameters for this purpose required less than 2 h. Our approach revealed a new list of targets, from which a new target, 104, also resulted in a single-movie solution.

By default, REyes collects 9 continuous rotation data sets; however, tilt series data completeness ultimately depends on crystal space group and orientation on the grid, which are not a priori knowledge. In this example, a single movie solution has been obtained from the third data set from Arctica/CETA-D system. The other 8 data sets could be merged to yield a high-quality structure as well. For example, without using target 104 data, we have successfully merged targets 103, 208, and 214, which produced an 82.7% complete solution with I/σ 3.9, *Rint* 37.10%, and $CC_{1/2}$ 96.7%.

Benchmarking Fully Autonomous MicroED. To benchmark the broader utility of a fully autonomous REyes pipeline, we examined four more crystalline structures: the beam-insensitive mineral grossular (**2**), vitamin B7 (biotin, **3**) with moderate beam sensitivity, a beam-sensitive peptide, AVAAGA (**4**), and the highly beam-sensitive Cu(*D*-Ser)$_2$ complex **5**. All four samples were first analyzed under identical settings at room temperature by using the F200C/Apollo microscope/camera configuration. Each molecular structure was autonomously solved *ab initio* from a single movie (Figure 4).

Grossular lacks uniformly crystalline particles, which typically require numerous hours for manual surveying. In contrast, REyes surveyed the grid and collected nine high-quality tilt series within 3 h. When applied to biotin (**3**), our pipeline identified multiple crystallites classified as "Good" diffraction. REyes yielded a data set with 98.6% completeness that phased *ab initio*, with 97.0% completeness after refinement, with an I/σ of 6.1.

The hexapeptide AVAAGA (**4**) and Cu(*D*-Ser)$_2$ complex **5**, in our experience, are challenging for acquisition at room temperature due to their beam sensitivity. REyes efficiently delivered single-movie solutions in under 3 h (Figure 4). The best AVAAGA peptide data set was 97.8% complete after refinement with an I/σ of 7.1. The most challenging sample studied at room temperature was Cu(*D*-Ser)$_2$ complex **5**. Despite its high beam sensitivity, REyes obtained a single movie solution from a 77.4% complete data set after refinement and an I/σ of 5.7.

The same samples, analyzed at cryogenic temperatures with an Arctica/CETA-D system, also yielded the expected structural outcomes. While the slower rotation rate and lower sensitivity of the CETA-D increased both sample surveying and tilt series acquisition times, the REyes approach was successful on this cost-effective and widely available detector. All 5 samples, (*S*,*S*)-salen ligand (**1**), grossular (**2**), biotin (**3**), AVAAGA peptide (**4**), and Cu(*D*-Ser)$_2$ (**5**), were successfully measured, with each compound producing a single movie solution in 6 h (for structure factors and details, see the Supporting Information). The longer acquisition time was primarily due to a slower rotation rate (0.12°/s for CETA-D vs 1°/s for Apollo) during tilt series data collection. The beam-

https://doi.org/10.1021/jacs.5c10751
J. Am. Chem. Soc. 2025, 147, 42299−42310

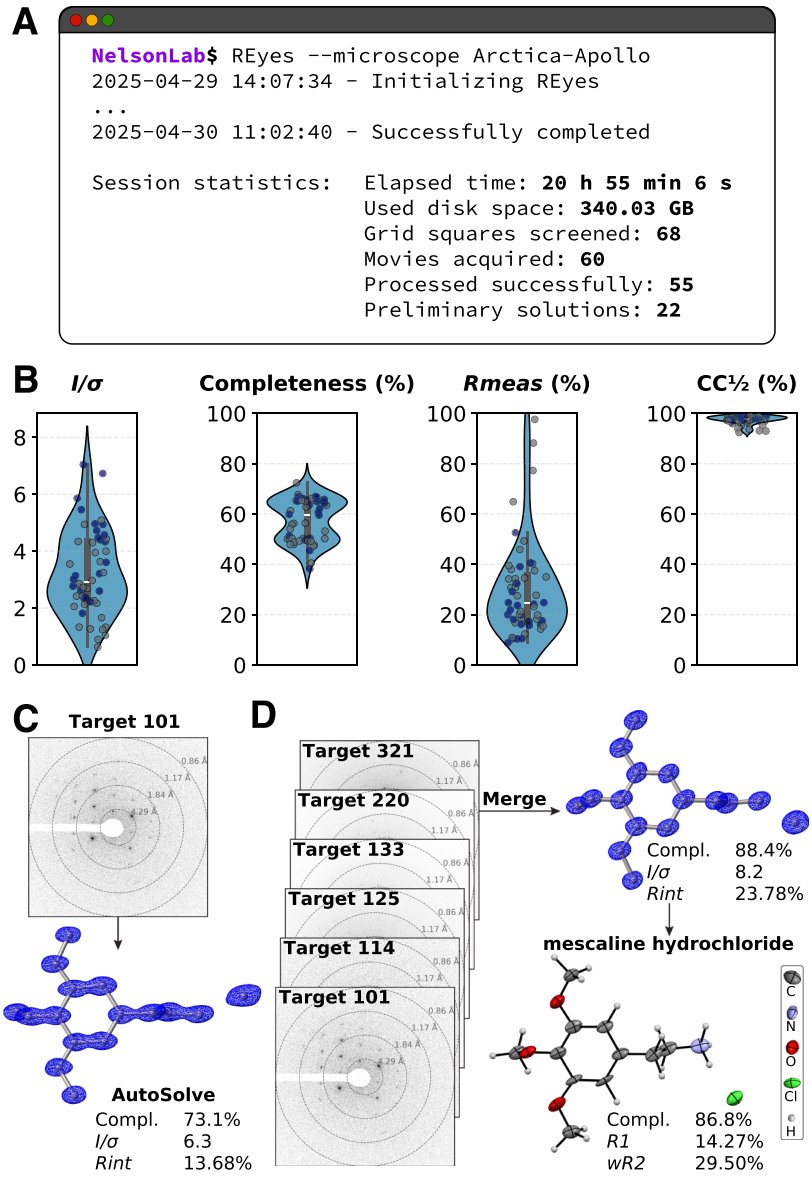


Figure 5. Autonomous microED workflow for cactus extract using REyes. (A) Generalized initialization of REyes and output of operations on an Arctica/Apollo system. (B) Violin plots of I/σ, completeness, *Rmeas*, and $CC_{1/2}$ across 54 successfully processed movies. Circles represent individual data set results, where navy blue circles resulted in successful *ab initio* phasing of an unknown compound from a cactus crude extract; box plots within the violins indicate median and interquartile ranges. (C) Diffraction pattern for target 101 resulted in the best preliminary phasing. (D) Merged REyes targets used for the final *ab initio* phasing and refinement of mescaline hydrochloride.

sensitive Cu(*D*-Ser)$_2$ (**5**), however, suffered radiation damage during slow, yet cryogenic, data collection, limiting achievable completeness to only 66.7% (77.4% with Apollo detector). The best structural model was obtained by refining against an analogous model from the Apollo data collected at room temperature. This underscores the importance of low-dose, high-speed acquisition strategies for beam-sensitive materials, where rapid data collection could significantly improve data quality even at room temperature compared to higher fluence, slow cryogenic data acquisition.

The REyes pipeline was further demonstrated on two 300 kV microscopes: a Tecnai TF-30/TVIPS and a Spectra 300C/CETA-D. REyes installation and optimization of diffraction processing parameters required less than 2 h, yielding a system ready for fully autonomous data acquisition. Using (*S*,*S*)-salen ligand (**1**) as a reference sample, each instrument autonomously collected 9 movies of comparable data quality to those obtained on 200 kV microscopes.

Next, we put REyes to the test, evaluating its ability to determine the structure of a complex NP: citrinovirin (**6**), isolated from *Trichoderma citrinoviride* and characterized by microED.[35] The sample was deposited onto a TEM grid and autonomously analyzed with REyes operating the Arctica/CETA-D system. One of 9 continuous rotation data sets, collected within 6 h, provided a solution with 98.4% completeness (for details, see the Supporting Information).

Autonomous Analysis of Crude Extract with Reyes. We next gauged REyes' ability to autonomously detect NPs in a crude extract of the so-called Argentine Saguaro Cactus, *Echinopsis terscheckii*, which was taxonomically verified by the supplier. Despite their broad geographic distribution and existing applications, cacti remain underexplored.[43]

https://doi.org/10.1021/jacs.5c10751
J. Am. Chem. Soc. 2025, 147, 42299−42310

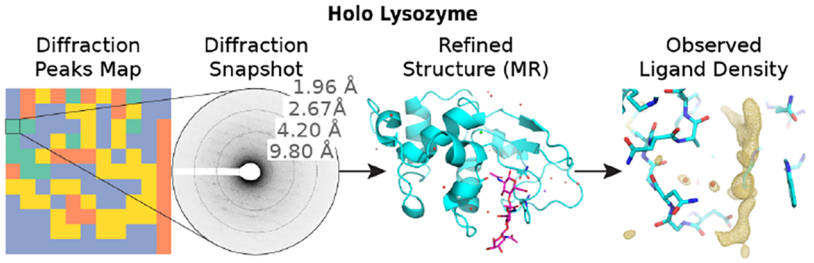


Figure 6. REyes, AutoProcess, molecular replacement, and refinement results of an automated microED acquisition of tetragonal holo-lysozyme. REyes "Quality" diffraction map of a grid square led to a single-movie solution, diffraction snapshot at 2.0 Å max resolution of the target selected by REyes using the Arctica/Apollo system, refined structure of lysozyme phased using molecular replacement, gold-mesh represents 3σ NAG_3 ligand in the F_o-F_c map.

The crude extract containing visible particulates was directly applied to a TEM grid. REyes was deployed to screen a 1 mm^2 area of the grid using an Arctica/Apollo. REyes autonomously and continuously screened 68 grid squares, captured 8228 diffraction snapshots, and acquired 60 continuous rotation data sets (1°/s over $a \pm 50°$ range) from the most promising crystalline targets, all in less than 21 h without human intervention (Figure 5A). These data sets were processed on-the-fly using the integrated AutoProcess and AutoSolve pipelines, resulting in 22 preliminary *ab initio* phasing solutions.

Unexpectedly, 43 of the 54 data sets corresponded to the same unit cell: $a = 38.6 \pm 0.8$ Å, $b = 5.13 \pm 0.02$ Å, $c = 12.87 \pm 0.05$ Å, $\alpha = 90°$, $\beta = 104.5 \pm 0.9°$, $\gamma = 90°$. From these, the 34 highest-quality data sets exhibited I/σ ranging from 2 to 5, completeness between ~40 and 70%, *Rmeas* values from 14–41%, and $CC_{1/2}$ values above 93% (Figure 5B). The remaining 10 of the 11 corresponded to the reduced unit cell parameters of the same crystal system, and they led to the structurally identical phasing solution. The final data set lacked sufficient quality to support a meaningful structural interpretation.

Among the successfully phased data sets, crystal target 101 yielded the highest-quality *ab initio* solution in space group *C*2/*c*, revealing a molecular framework consistent with a 3,4,5-trimethoxyphenethyl core, a hallmark of the mescaline alkaloid family (Figure 5C). To improve completeness, six data sets were merged using crystal 101 as a reference, although preferred particle orientation on the grid limited the final 88.4% completeness (Figure 5D). Initial phasing indicated a solution in a monoclinic space group *C*2/*c*, and structure refinement ultimately yielded a solution consistent with mescaline hydrochloride (**7**).[44,45]

The potential presence of mescaline protoalkaloids in the *Echinopsis* genus has been previously reported.[46] Liquid chromatography–high-resolution mass spectrometry (LC-HRMS) analysis of the crude extract revealed several features with *m*/*z* values corresponding to mescaline analogues. Accordingly, our proposed structure of alkaloid **7** underscores the transformative potential of REyes as a self-driving microED platform for the structure elucidation of natural products in mixtures.

REyes in Protein Structure Determination. Given the promise of REyes for structure elucidation of small molecules and materials, we next evaluated its ability to determine biomacromolecular structures. As a proof-of-concept, we applied the same autonomous acquisition and target selection logic to tetragonal crystals of the venerable protein standard lysozyme in complex with tri-*N*-acetyl-D-glucosamine (NAG_3) (**9**).

To compensate for a higher background and dimmer reflections expected from protein crystal diffraction, we adjusted the electron beam and SerialEM parameters within the REyes suite. Specifically, beam flux was increased approximately 2-fold, a selected area aperture was permanently inserted, and the step size of the diffraction mapping was decreased from 5 to 3 μm to maximize spatial coverage, but no modifications were made to the Python-based components of REyes.

High-quality diffraction snapshots were observed throughout the scanned area, which consisted of 25 grid squares. Given the overall higher number but reduced intensity of protein diffraction peaks, REyes target selection was guided mainly by peak count, maintaining high DQI. From this analysis, a single-movie solution was obtained from target 203, which was identified in grid square #7 (Figure 6). The data were indexed to a tetragonal unit cell: $a = b = 79.57$ Å, $c = 39.87$ Å, and $\alpha = \beta = \gamma = 90°$, in the *P*422 space group.

The acquired data set was autonomously processed using AutoProcess, which successfully indexed and integrated the protein microED data. Phasing was performed manually via molecular replacement (MR) in space group $P4_32_12$, using a lysozyme model lacking a ligand. A subsequently refined model at 2.2 Å confirmed occupancy of the bound NAG_3 ligand, which was clearly resolved in the electrostatic potential map (Figure 6).

This result demonstrates that REyes could be extended beyond small molecules to enable the structure determination of proteins, with planned integration of MR into the fully autonomous workflow. Differences in diffraction patterns between small molecules and macromolecules likewise require future fine-tuning of diffraction classification algorithms. Meanwhile, the current generation of REyes already supports robust autonomous acquisition and analysis of crystalline proteins.

Assessing the Diffraction Quality of REyes Data. We evaluated the ability of REyes to classify diffraction with two data sets acquired on the F200C/Apollo: (*S*,*S*)-salen ligand (**1**) and biotin (**3**). Classification follows precise numerical thresholds applied through Gaussian filters for peak detection and FT pattern quality analysis, adjusted to each microscope/camera pair. These thresholds were designed as intuitive numerical parameters that either do not require adjustment or can be tuned upon REyes installation with minimal to no prior experience in microED acquisition. In addition, the central 25% of each image is masked during peak detection, ensuring

https://doi.org/10.1021/jacs.5c10751
J. Am. Chem. Soc. 2025, 147, 42299–42310

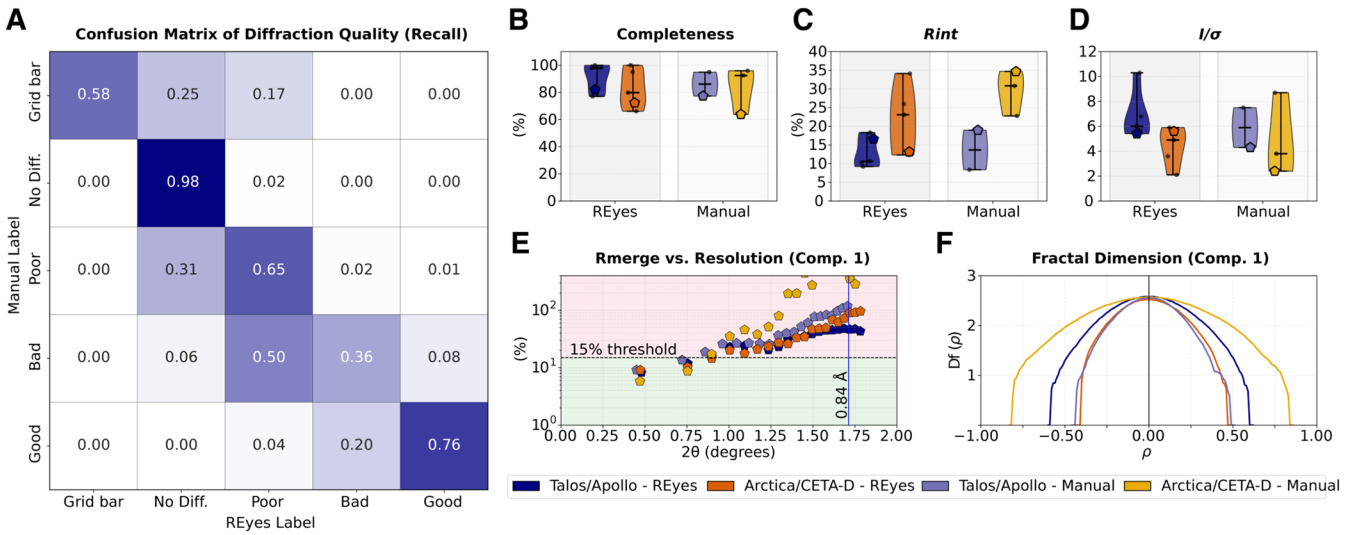


Figure 7. Comparison of diffraction data quality metrics obtained by REyes. (A) Row-normalized (recall) confusion matrix showing how each manually assigned category (rows) maps to REyes classifications (columns). (B–D) Violin plots comparing (B) completeness, (C) *Rint*, and (D) I/σ of solutions from single microED movies obtained by REyes and acquired manually. Pentagon point represents (*S*,*S*)-salen ligand **1**. (E) *Rmerge* values plotted against 2θ resolution. (F) Fractal dimension measurements for REyes versus manual data collection.

that the "Good" class reflects high-resolution features of the diffraction pattern rather than the low-resolution signal.

REyes achieves substantial agreement with manual classification, Cohen's Kappa[47] of 0.66, while demonstrating effective performance for the "Good" diffraction class. Due to high imbalance in the data and a dominating "No diffraction" class performance evaluation using precision, recall, and F1-score metrics[48] reveal that REyes prioritizes recall over precision for high-quality targets, achieving 76% recall, 65% precision, and an F1-score of 0.70 for the "Good" class. This design aligns with practical microED acquisition goals, where detecting most high-quality targets (high recall) is more critical than avoiding all false positives (high precision). Similar principles are well established in diagnostic science and imbalanced classification literature, where the cost of overlooking true positives often outweighs the inclusion of occasional false positives.[49−51] The normalized combined confusion matrix reveals that most misclassifications occur between adjacent quality categories, with only 8% of images (18 out of 223) manually labeled as "Bad" being classified as "Good" (Figure 7A).

The biggest classification challenge occurs for "Poor" and "Bad" categories. For the (*S*,*S*)-salen ligand **1** data set, over half of the manually labeled "Bad" samples are classified as "Poor." Since both categories are likely to represent suboptimal lattices, this approach prioritizes processing efficiency at the expense of tolerating an observed classification overlap. The substantial class imbalance caused by the overpopulated "No diffraction" category, representing 91.8 and 76.1% of the respective data sets, is explained by the intentional relative sparsity of grids. This favors the diffraction of isolated particles with confidence, since the developed model effectively identifies images in the "No diffraction" category (F1 scores of 0.99 and 0.97). REyes applies this rubric across all samples, independent of the intrinsic quality of crystallite in the sample, ensuring comparable autonomous microED data collection.

By favoring confident identification of high-quality patterns and minimizing the risk of overlooking them, REyes ensures efficient and reproducible data collection across diverse samples. This enables consistent microED performance even in sparse or challenging grids without requiring expert oversight.

Comparing REyes to Human-Driven MicroED Data Collection. In our experience, failure of *ab initio* structure determination from a single continuous rotation movie with resolution higher than 1.0−1.2 Å is typically due to insufficient completeness of diffraction data. We assessed the performance of REyes in both high and low completeness regimes and, importantly, compared its performance to that of microED practitioners. We compared data quality and structural outcomes for data sets acquired using REyes or manually collected by a human operator on both a CETA-D and Apollo direct electron detectors under comparable conditions (Figure 7B−D).[52] The violin plots comparing data for benchmark samples suggest an unbiased advantage in using REyes.

Assessing data collected from (*S*,*S*)-salen ligand (**1**) as a representative system (for other data comparisons, see the Supporting Information), REyes data from the Apollo detector achieved 5−10% higher completeness relative to their manually collected counterparts (Figure 7B). This is surprising given that, in principle, completeness is primarily determined by crystal orientation and should be independent of the data acquisition workflow. The difference likely stems from more comprehensive grid coverage achieved with REyes and the unbiased diffraction quality-driven target selection strategy compared to the more biased, human effort of visual particle targeting.

The internal consistency of data, as measured by the internal consistency of equivalent reflections R factor (*Rint*), provides a metric for data reliability. Data sets acquired with REyes showed a 3−18% reduction in *Rint* compared to manually collected data (Figure 7C). This enhancement is also subject to the unbiased selection of diffraction features by REyes, rather than the human selection of particles in real space. REyes data was also notably better in its signal-to-noise ratio, with I/σ values 2−4 units higher than those obtained from manual acquisition (Figure 7D). We also assessed merging R factors (*Rmerge*) across data sets, finding lower *Rmerge* values

https://doi.org/10.1021/jacs.5c10751
J. Am. Chem. Soc. 2025, 147, 42299−42310

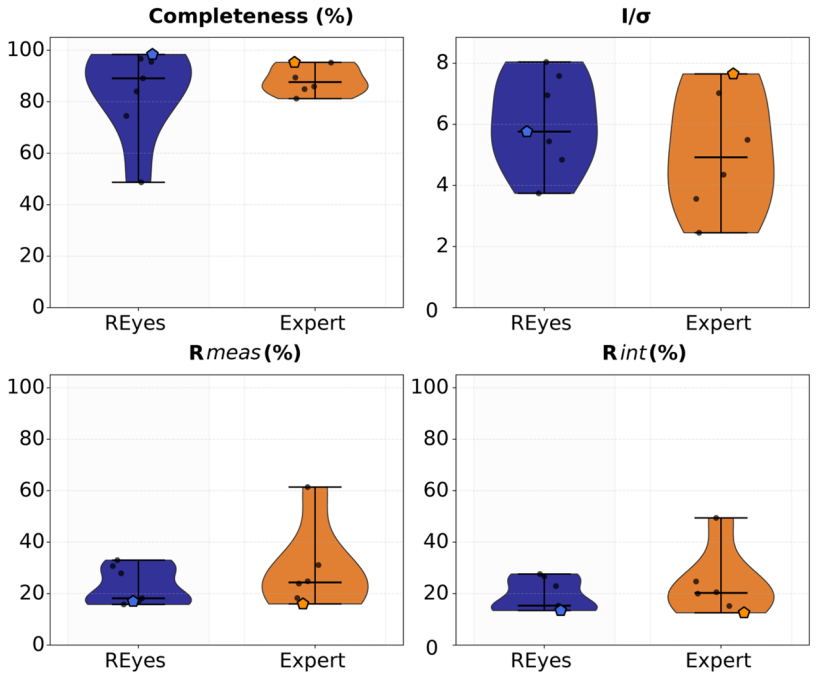


Figure 8. Blind REyes vs Expert performance. Violin plots comparing completeness, I/σ, *Rint*, and *Rmeas* from the top five microED movies collected by REyes and the Expert from the same biotin grid. The pentagon symbol marks the best data set.

across REyes data sets. This underscores the robustness of diffraction classification and autonomous target selection compared with conventional manual workflows (Figure 7E).

Lastly, we assessed the quality of the determined structures by examining residual electrostatic potential distributions using fractal dimension analysis.[53] In all four test cases, residual maps approximated Gaussian distributions, which is consistent with unbiased structural models. A REyes data set acquired using a CETA-D camera produced steeper fractal plots, indicative of higher model fidelity (Figure 7F). A subtle exception was observed for a REyes data set collected with the Apollo detector, which exhibited slightly shallower fractal profiles compared to the manually collected data, although this is not the case when we compare data for biotin (**3**), AVAAGA peptide (**4**), and Cu(*D*-Ser)$_2$ (**5**).

One could attribute individual discrepancies to acquisition bias, intrinsic differences in crystal quality, and acquisition temperature, as distinct crystals were analyzed on each platform. However, together, these results demonstrate that REyes not only accelerates data acquisition but also enables consistency and reproducibility, while maintaining and often enhancing the quality of microED data, compared with manual acquisition.

Out of the 214 collected diffraction movies, 63.6% were successfully indexed. Indexing success correlates with diffraction quality: data sets with LQP $\leq$ 10 showed only ~40% success, whereas those with LQP > 10 reached 70−90%. Similarly, data sets with DQI $\leq$ 1 indexed at ~50% success, while DQI > 1 yielded progressively higher rates, approaching ~90% in the best bins. Among the successfully indexed data sets (n = 136), both LQP and DQI correlate with improved data quality: $CC_{1/2}$ and I/σ increased, while *Rmeas* decreased with higher values of either metric. Phasing success across small-molecule data sets (n = 120) was 38.3%, but exceeded 50% for DQI > 6.2, underscoring that autocorrelation-based metrics are predictive of downstream structure solution. These results demonstrate that higher-quality data originate from targets with higher LQP and DQI values obtained from the original diffraction snapshots (see the Supporting Information).

To directly compare REyes with a human operator under identical conditions, we performed a blind experiment using biotin as a model system. A team member prepared and loaded the grid, after which data were collected in separate sessions by an experienced operator ("Expert") and by REyes, both using the same Arctica/Apollo setup and identical processing AutoProcess/AutoSolve pipelines. The Expert obtained a preliminary solution in under 1 h from 6 movies. A standard REyes session evaluating 9 grid squares required just over 3 h to collect 12 movies and reach a solution, reflecting the higher speed of human-driven acquisition. REyes yielded 7 correctly indexed data sets with a slightly higher mean I/σ (6.1 vs 5.1). A direct comparison of the top five data sets from each session (Figure 8) shows overlapping distributions of data quality, with the Expert maintaining a slight edge but REyes producing results of equivalent reliability. For both REyes and Expert, the best single-movie solutions resulted in >95% completeness, I/σ > 5, *Rmeas* < 20%, *Rint* < 15%. This experiment confirms that although an expert human operator might arrive at a structure solution faster, REyes already achieves data quality on par with an Expert, and in some cases surpasses them. This underscores the potential for REyes to democratize high-quality microED data collection.

CONCLUSIONS

REyes introduces a fully autonomous, diffraction-guided workflow for microED data acquisition that eliminates the need for human intervention from target identification through structural solution. By leveraging real-time diffraction mapping and sample-independent classification, REyes ensures the selective targeting of high-quality crystalline data. The performance of the system was validated across chemically

https://doi.org/10.1021/jacs.5c10751
J. Am. Chem. Soc. 2025, 147, 42299−42310

and structurally diverse compounds, with all structures solved from single data sets, demonstrating both speed and precision. The utility of this approach is further demonstrated by the recent implementation of REyes-like protocols in other emerging packages.[54] The diffraction classification model ensures robust decision-making and efficient use of instrument time, even for challenging or beam-sensitive samples, including proteins. This work lays the foundation for scalable, fully self-driving molecular structure elucidation, unlocking new possibilities in the discovery of materials, biomolecules, and pharmaceuticals.

■ ASSOCIATED CONTENT

Data Availability Statement

MicroED structure of the lysozyme-ligand complex is available via PDB entry: 9P6R. All other data are provided in the Supporting Information. REyes Python package, associated SerialEM script suite, installation manual, user guides, support tools, and hyperlink to the raw data are available at https://github.com/theNelsonLab/pyREyes. The example raw and processed data set for (*S*,*S*)-salen ligand **1** are available at 10.5281/zenodo.16971798.

Supporting Information

The Supporting Information is available free of charge at https://pubs.acs.org/doi/10.1021/jacs.5c10751.

Experimental details, REyes data, and microED structural data (PDF)

Accession Codes

Deposition Numbers 2449546−2449550, 2449554−2449556, and 2449594−2449604 contain the supplementary crystallographic data for this paper. These data can be obtained free of charge via the joint Cambridge Crystallographic Data Centre (CCDC) and Fachinformationszentrum Karlsruhe Access Structures service.

■ AUTHOR INFORMATION

Corresponding Authors

Hosea M. Nelson − *Division of Chemistry and Chemical Engineering, California Institute of Technology, Pasadena, California 91125, United States;* orcid.org/0000-0002-4666-2793; Email: hosea@caltech.edu

Jose A. Rodríguez − *Department of Chemistry and Biochemistry, University of California, Los Angeles, Los Angeles, California 90095, United States; UCLA-DOE Institute for Genomics & Proteomics, University of California, Los Angeles, Los Angeles, California 90095, United States;* orcid.org/0000-0002-0248-4964; Email: jrodriguez@mbi.ucla.edu

Vincent Lavallo − *Department of Chemistry, University of California, Riverside, Riverside, California 92521, United States;* orcid.org/0000-0001-8945-3038; Email: vincent.lavallo@ucr.edu

Authors

Dmitry B. Eremin − *Division of Chemistry and Chemical Engineering, California Institute of Technology, Pasadena, California 91125, United States;* orcid.org/0000-0003-2946-5293

Kunal K. Jha − *Division of Chemistry and Chemical Engineering, California Institute of Technology, Pasadena, California 91125, United States*

David A. Delgadillo − *Division of Chemistry and Chemical Engineering, California Institute of Technology, Pasadena, California 91125, United States;* orcid.org/0000-0002-0897-4470

Hongyu Zhang − *Division of Chemistry and Chemical Engineering, California Institute of Technology, Pasadena, California 91125, United States*

Samuel H. Foxman − *Division of Chemistry and Chemical Engineering, California Institute of Technology, Pasadena, California 91125, United States*

Samuel N. Johnson − *Division of Chemistry and Chemical Engineering, California Institute of Technology, Pasadena, California 91125, United States*

Niko W. Vlahakis − *Department of Chemistry and Biochemistry, University of California, Los Angeles, Los Angeles, California 90095, United States*

Duilio Cascio − *Department of Chemistry and Biochemistry, University of California, Los Angeles, Los Angeles, California 90095, United States; UCLA-DOE Institute for Genomics & Proteomics, University of California, Los Angeles, Los Angeles, California 90095, United States*

Complete contact information is available at: https://pubs.acs.org/10.1021/jacs.5c10751

Author Contributions

All authors approved the final version of the manuscript.

Notes

D.B.E., H.Z., J.A.R., and H.M.N. have filed a provisional patent, application number CIT-9295-P2 on 5/8/2025. In addition, J.A.R. and H.M.N. are equity stakeholders in MedStruc Inc. The authors declare no competing financial interest.

■ ACKNOWLEDGMENTS

Dedicated to the memory of Prof. George M. Sheldrick, in honor of his lifelong contributions to science. The authors thank Alex Lisker (UCLA) for computational infrastructure management; Cameron Flowers (UCLA) for the samples of lysozyme crystals; Dr. William Palfey and Prof. George Rossman (Caltech) for the samples of grossular; Dr. Adam Stieg, Dr. Matthew Mecklenburg, and Dr. Jungyoun Cho (CNSI/UCLA) for providing access to Spectra 300C microscope; Dr. Scott Virgil (Caltech) and the Center for Catalysis and Chemical Synthesis for the LC-HRMS infrastructure and support; Katya Kadyshevskaya (USC) for the design of REyes icon; and Dr. Jessica Burch and Isabel Hernandez Rodriguez for their pioneering work on computer vision-based microED workflows. The authors thank the Resnick High Performance Computing Center for providing computational resources. The code development was supported by Claude (Anthropic) and ChatGPT (OpenAI) resources. ChatGPT (OpenAI) was used to assist with language editing and proofreading of this manuscript. Figure 1 and TOC were created with BioRender.com. Development of the platform for diffraction data labeling has been supported by the NSF CCI Center for Computer Assisted Synthesis (CHE-1925607). Structure elucidation of natural products has been supported by NIH NCCIH (R01AT011990) and Howard Hughes Medical Institute Emerging Pathogens Initiative (HHMI-EPI). Use of Spectra 300C was supported by the BioPACIFIC Materials Innovation Platform of the NSF (DMR-1933487). V.L. is grateful for partial NSF support of this project (CHE-2003418).

■ ABBREVIATIONS

CryoEM, cryogenic electron microscopy; DQI, diffraction quality index; FT, Fourier transform; LC−HRMS, liquid chromatography−high-resolution mass spectrometry; LQP, lattice-quality peak; microED, microcrystal electron diffraction; MOF, metal−organic framework; NP, natural product; REyes, reciprocal eyes; SCXRD, single-crystal X-ray diffraction; TEM, transmission electron microscope

■ REFERENCES

(1) Kühlbrandt, W. The Resolution Revolution. *Science* **2014**, *343* (6178), 1443−1444.

(2) Dimmeler, E.; Vossen, O.; Schröder, R. R. Determination of Lattice-transform Density Profiles for Multilayered Three-dimensional Microcrystals in Electron Crystallography. *J. Appl. Crystallogr.* **2000**, *33* (4), 1102−1112.

(3) Jones, C. G.; Martynowycz, M. W.; Hattne, J.; Fulton, T. J.; Stoltz, B. M.; Rodriguez, J. A.; Nelson, H. M.; Gonen, T. The CryoEM Method MicroED as a Powerful Tool for Small Molecule Structure Determination. *ACS Cent. Sci.* **2018**, *4* (11), 1587−1592.

(4) Kolb, U.; Matveeva, G. N. Electron Crystallography on Polymorphic Organics. *Z. Kristallogr. - Cryst. Mater.* **2003**, *218* (4), 259−268.

(5) Delgadillo, D. A.; Burch, J. E.; Kim, L. J.; de Moraes, L. S.; Niwa, K.; Williams, J.; Tang, M. J.; Lavallo, V. G.; Chhetri, B. K.; Jones, C. G.; Rodriguez, I. H.; Signore, J. A.; Marquez, L.; Bhanushali, R.; Woo, S.; Kubanek, J.; Quave, C.; Tang, Y.; Nelson, H. M. High-Throughput Identification of Crystalline Natural Products from Crude Extracts Enabled by Microarray Technology and microED. *ACS Cent. Sci.* **2024**, *10* (1), 176−183.

(6) Paik, J. Lenacapavir: First Approval. *Drugs* **2022**, *82* (14), 1499−1504.

(7) Luo, Y.; Wang, B.; Smeets, S.; Sun, J.; Yang, W.; Zou, X. High-Throughput Phase Elucidation of Polycrystalline Materials Using Serial Rotation Electron Diffraction. *Nat. Chem.* **2023**, *15* (4), 483−490.

(8) Jones, C. G.; Asay, M.; Kim, L. J.; Kleinsasser, J. F.; Saha, A.; Fulton, T. J.; Berkley, K. R.; Cascio, D.; Malyutin, A. G.; Conley, M. P.; Stoltz, B. M.; Lavallo, V.; Rodríguez, J. A.; Nelson, H. M. Characterization of Reactive Organometallic Species via MicroED. *ACS Cent. Sci.* **2019**, *5* (9), 1507−1513.

(9) Motaln, K.; Gurung, K.; Brázda, P.; Kokalj, A.; Radan, K.; Dragomir, M.; Žemva, B.; Palatinus, L.; Lozinšek, M. Reactive Noble-Gas Compounds Explored by 3D Electron Diffraction: XeF_2−MnF_4 Adducts and a Facile Sample Handling Procedure. *ACS Cent. Sci.* **2024**, *10* (9), 1733−1741.

(10) Gemmi, M.; Mugnaioli, E.; Gorelik, T. E.; Kolb, U.; Palatinus, L.; Boullay, P.; Hovmöller, S.; Abrahams, J. P. 3D Electron Diffraction: The Nanocrystallography Revolution. *ACS Cent. Sci.* **2019**, *5* (8), 1315−1329.

(11) Delgadillo, D. A.; Wu, L.; Wang, C.; Zhang, Y.; Jha, K. K.; Burch, J. E.; de Moraes, L. S.; Rodriguez, I. H.; Tang, M. J.; Bills, G. F.; Tu, B. P.; Tang, Y.; Nelson, H. M. Microcrystal Electron Diffraction-Guided Discovery of Fungal Metabolites. 26158−26164. DOI: 10.1021/jacs.5c01466.

(12) Abad, A. N. D.; Seshadri, K.; Ohashi, M.; Delgadillo, D. A.; de Moraes, L. S.; Nagasawa, K. K.; Liu, M.; Johnson, S.; Nelson, H. M.; Tang, Y. Discovery and Characterization of Pyridoxal 5′-Phosphate-Dependent Cycloleucine Synthases. *J. Am. Chem. Soc.* **2024**, *146* (21), 14672−14684.

(13) Park, J.; Li, Y.; Moon, K.; Han, E. J.; Lee, S. R.; Seyedsayamdost, M. R. Structural Elucidation of Cryptic Algaecides in Marine Algal-Bacterial Symbioses by NMR Spectroscopy and MicroED. *Angew. Chem., Int. Ed.* **2022**, *61* (4), No. e202114022.

(14) Anderson, C. L.; Li, H.; Jones, C. G.; Teat, S. J.; Settineri, N. S.; Dailing, E. A.; Liang, J.; Mao, H.; Yang, C.; Klivansky, L. M.; Li, X.; Reimer, J. A.; Nelson, H. M.; Liu, Y. Solution-Processable and Functionalizable Ultra-High Molecular Weight Polymers via Topochemical Synthesis. *Nat. Commun.* **2021**, *12* (1), No. 6818.

(15) De Bolòs, E.; Martínez-Abadía, M.; Hernández-Culebras, F.; Haymaker, A.; Swain, K.; Strutyński, K.; Weare, B. L.; Castells-Gil, J.; Padial, N. M.; Martí-Gastaldo, C.; Khlobystov, A. N.; Saeki, A.; Melle-Franco, M.; Nannenga, B. L.; Mateo-Alonso, A. A Crystalline 1D Dynamic Covalent Polymer. *J. Am. Chem. Soc.* **2022**, *144* (34), 15443−15450.

(16) Meng, Z.; Stolz, R. M.; Moraes, L. S. D.; Jones, C. G.; Eagleton, A. M.; Nelson, H. M.; Mirica, K. A. Gas-Induced Electrical and Magnetic Modulation of Two-Dimensional Conductive Metal−Organic Framework. *Angew. Chem., Int. Ed.* **2024**, *63* (24), No. e202404290.

(17) Banihashemi, F.; Bu, G.; Thaker, A.; Williams, D.; Lin, J. Y. S.; Nannenga, B. L. Beam-Sensitive Metal-Organic Framework Structure Determination by Microcrystal Electron Diffraction. *Ultramicroscopy* **2020**, *216*, No. 113048.

(18) Ravin, K.; Sarver, P.; Dinakar, B.; Palatinus, L.; Müller, P.; Oppenheim, J.; Dincă, M. High-Connectivity Triazolate-Based Metal−Organic Framework for Water Harvesting. *J. Am. Chem. Soc.* **2025**, *147* (13), 11407−11411.

(19) Das, S.; Al-Miqdadi, O.; Cheng, W. W.; Tidey, J. P.; Walker, M.; Pandey, G. C.; Walton, R. I. Fe-2,5-furandicarboxylate Metal Organic Frameworks with Rare Building Blocks and a Ligand That Can Be Biomass-Derived as Effective Catalysts for Selective Nitroarene Reduction. *ChemSusChem* **2025**, *18*, No. e202500120.

(20) Prasad, R. R. R.; Boyadjieva, S. S.; Zhou, G.; Tan, J.; Firth, F. C. N.; Ling, S.; Huang, Z.; Cliffe, M. J.; Foster, J. A.; Forgan, R. S. Modulated Self-Assembly of Catalytically Active Metal−Organic Nanosheets Containing Zr_6 Clusters and Dicarboxylate Ligands. *ACS Appl. Mater. Interfaces* **2024**, *16* (14), 17812−17820.

(21) Samkian, A. E.; Kiel, G. R.; Jones, C. G.; Bergman, H. M.; Oktawiec, J.; Nelson, H. M.; Tilley, T. D. Elucidation of Diverse Solid-State Packing in a Family of Electron-Deficient Expanded Helicenes via Microcrystal Electron Diffraction (MicroED). *Angew. Chem., Int. Ed.* **2021**, *60* (5), 2493−2499.

(22) Zee, C.-T.; Glynn, C.; Gallagher-Jones, M.; Miao, J.; Santiago, C. G.; Cascio, D.; Gonen, T.; Sawaya, M. R.; Rodriguez, J. A. Homochiral and Racemic MicroED Structures of a Peptide Repeat from the Ice-Nucleation Protein InaZ. *IUCrJ.* **2019**, *6* (2), 197−205.

(23) Danelius, E.; Porter, N. J.; Unge, J.; Arnold, F. H.; Gonen, T. MicroED Structure of a Protoglobin Reactive Carbene Intermediate. *J. Am. Chem. Soc.* **2023**, *145* (13), 7159−7165.

(24) Klar, P. B.; Waterman, D. G.; Gruene, T.; Mullick, D.; Song, Y.; Gilchrist, J. B.; Owen, C. D.; Wen, W.; Biran, I.; Houben, L.; Regev-Rudzki, N.; Dzikowski, R.; Marom, N.; Palatinus, L.; Zhang, P.; Leiserowitz, L.; Elbaum, M. Cryo-Tomography and 3D Electron Diffraction Reveal the Polar Habit and Chiral Structure of the Malaria Pigment Crystal Hemozoin. *ACS Cent. Sci.* **2024**, *10* (8), 1504−1514.

(25) Vlahakis, N. W.; Flowers, C. W.; Liu, M.; Agdanowski, M. P.; Johnson, S.; Summers, J. A.; Jacobs, L. M. C.; Keyser, C.; Russell, P.; Rose, S. L.; Orlans, J.; Adhami, N.; Chen, Y.; Sawaya, M. R.; Basu, S.; de Sanctis, D.; Chen, Y.; Wakatsuki, S.; Nelson, H. M.; Loo, J. A.; Tang, Y.; Rodriguez, J. A. Combining MicroED and Native Mass Spectrometry for Structural Discovery of Enzyme−Small Molecule Complexes. *Proc. Natl. Acad. Sci. U.S.A.* **2025**, *122* (31), No. e2503780122.

(26) Clabbers, M. T. B.; Hattne, J.; Martynowycz, M. W.; Gonen, T. Energy Filtering Enables Macromolecular MicroED Data at Sub-Atomic Resolution. *Nat. Commun.* **2025**, *16* (1), No. 2247.

(27) Plana-Ruiz, S.; Krysiak, Y.; Portillo, J.; Alig, E.; Estradé, S.; Peiró, F.; Kolb, U. Fast-ADT: A Fast and Automated Electron Diffraction Tomography Setup for Structure Determination and Refinement. *Ultramicroscopy* **2020**, *211*, No. 112951.

(28) Scherer, S.; Kowal, J.; Chami, M.; Dandey, V.; Arheit, M.; Ringler, P.; Stahlberg, H. 2dx_automator: Implementation of a Semiautomatic High-Throughput High-Resolution Cryo-Electron Crystallography Pipeline. *J. Struct. Biol.* **2014**, *186* (2), 302−307.

(29) Wang, B.; Zou, X.; Smeets, S. Automated Serial Rotation Electron Diffraction Combined with Cluster Analysis: An Efficient Multi-Crystal Workflow for Structure Determination. *IUCrJ* **2019**, *6* (Pt 5), 854−867.
(30) Cichocka, M. O.; Ångström, J.; Wang, B.; Zou, X.; Smeets, S. High-Throughput Continuous Rotation Electron Diffraction Data Acquisition via Software Automation. *J. Appl. Crystallogr.* **2018**, *51* (6), 1652−1661.
(31) Wan, W.; Sun, J.; Su, J.; Hovmöller, S.; Zou, X. Three-Dimensional Rotation Electron Diffraction: Software RED for Automated Data Collection and Data Processing. *J. Appl. Crystallogr.* **2013**, *46* (6), 1863−1873.
(32) Bücker, R.; Hogan-Lamarre, P.; Miller, R. J. D. Serial Electron Diffraction Data Processing With Diffractem and CrystFEL. *Front. Mol. Biosci.* **2021**, *8*, No. 624264.
(33) Lin, J.; Gallenito, M. J.; Hattne, J.; Gonen, T. Ligand Screening and Discovery Using Cocktail Soaking and Automated Microcrystal Electron Diffraction. *ChemMedChem* **2025**, *20*, No. e2500156.
(34) Hogan-Lamarre, P.; Luo, Y.; Bücker, R.; Miller, R. J. D.; Zou, X. STEM SerialED: Achieving High-Resolution Data for *Ab Initio* Structure Determination of Beam-Sensitive Nanocrystalline Materials. *IUCrJ* **2024**, *11* (Pt1), 62−72.
(35) Unge, J.; Lin, J.; Weaver, S. J.; Her, A. S.; Gonen, T. Compositional Analysis of Complex Mixtures Using Automatic MicroED Data Collection. *Adv. Sci.* **2024**, *11* (23), No. 2400081.
(36) Eremin, D. E.; Zhang, H.; Rodríguez, J. A.; Nelson, H. M. *pyREyes*, GitHub, 2025. https://github.com/theNelsonLab/pyREyes.
(37) Patterson, A. L. A Fourier Series Method for the Determination of the Components of Interatomic Distances in Crystals. *Phys. Rev.* **1934**, *46* (5), 372−376.
(38) Wang, J.; Kamtekar, S.; Berman, A. J.; Steitz, T. A. Correction of X-Ray Intensities from Single Crystals Containing Lattice-Translocation Defects. *Acta Crystallogr., Sect. D: Biol. Crystallogr.* **2005**, *61* (1), 67−74.
(39) Lovelace, J. J.; Borgstahl, G. E. O. Characterizing Pathological Imperfections in Macromolecular Crystals: Lattice Disorders and Modulations. *Crystallogr. Rev.* **2020**, *26* (1), 3−50.
(40) Aguiar, J. A.; Gong, M. L.; Unocic, R. R.; Tasdizen, T.; Miller, B. D. Decoding Crystallography from High-Resolution Electron Imaging and Diffraction Datasets with Deep Learning. *Sci. Adv.* **2019**, *5* (10), No. eaaw1949.
(41) Deng, L.; Jacobsen, E. N. A Practical, Highly Enantioselective Synthesis of the Taxol Side Chain via Asymmetric Catalysis. *J. Org. Chem.* **1992**, *57* (15), 4320−4323.
(42) Eremin, D. E.; Foxman, S. H.; Burch, J. E.; Nelson, H. M. *AutoProcess 2.0.*, GitHub, 2025 https://github.com/theNelsonLab/autoprocess.
(43) Anderson, F. E. *The Cactus Family*; Timber Press, 2001.
(44) Tsoucaris, D.; de Rango, C.; Tsoucaris, G.; Zelwer, C.; Parthasarathy, R.; Cole, F. E. 1(2-Aminoethyl) 3,4,5-Trimethoxy-benzene (Mescaline) Hydrochloride, $C_{11}H_{18}ClNO_3$. *Cryst. Struct. Commun.* **1973**, *2*, 193−196.
(45) Ernst, S. R.; Cagle, F. W. Crystal Data for Some Mescaline Salts. *J. Appl. Crystallogr.* **1974**, *7* (1), 88−90.
(46) Reti, L.; Castrillón, J. A. Cactus Alkaloids. I. *Trichocereus Terscheckii* (Parmentier) Britton and Rose. *J. Am. Chem. Soc.* **1951**, *73* (4), 1767−1769.
(47) Warrens, M. J. New Interpretations of Cohen's Kappa. *J. Math.* **2014**, *2014* (1), No. 203907.
(48) Powers, D. M. W. Evaluation: From Precision, Recall and F-Measure to ROC, Informedness, Markedness & Correlation. *J. Mach. Learn. Technol.* **2011**, *2*, 37−63.
(49) Coley, C. W.; Eyke, N. S.; Jensen, K. F. Autonomous Discovery in the Chemical Sciences Part I: Progress. *Angew. Chem., Int. Ed.* **2020**, *59* (51), 22858−22893.
(50) Saito, T.; Rehmsmeier, M. The Precision-Recall Plot Is More Informative than the ROC Plot When Evaluating Binary Classifiers on Imbalanced Datasets. *PLoS One* **2015**, *10* (3), No. e0118432.
(51) U.S. Food and Drug Administration. *Statistical Guidance on Reporting Results from Studies Evaluating Diagnostic Tests.*; U.S. Department of Health and Human Services, 2007; FDA, https://www.fda.gov/media/71147/download. (accessed 2025).
(52) Evans, P. Scaling and Assessment of Data Quality. *Acta Crystallogr., Sect. D: Biol. Crystallogr.* **2006**, *62* (1), 72−82.
(53) Meindl, K.; Henn, J. Foundations of Residual-Density Analysis. *Acta Crystallogr., Sect. A: Found. Crystallogr.* **2008**, *64* (3), 404−418.
(54) Hofer, G.; Wang, L.; Pacoste, L.; Hager, P.; Fonjallaz, A.; Williams, L.; Hutchinson, E. S.; Palma, M. D.; Stenmark, P.; Worral, J.; Steiner, R. A.; Xu, H.; Zou, X.Continuous Serial Electron Diffraction for High Quality Protein Structures *bioRxiv* 2025. DOI: 10.1101/2025.09.14.676192.

